Appl. Math. Mech. -Engl. Ed., **41**(5), 753–768 (2020)

Applied Mathematics and Mechanics (English Edition)

https://doi.org/10.1007/s10483-020-2602-8

Chebyshev spectral variational integrator and applications*

Zhonggui YI[1], Baozeng YUE[1,†], Mingle DENG[2]

1. School of Aerospace Engineering, Beijing Institute of Technology, Beijing 100081, China;
2. China Academy of Space Technology, Beijing 100094, China

(Received Nov. 23, 2019 / Revised Feb. 5, 2020)

Abstract The Chebyshev spectral variational integrator (CSVI) is presented in this paper. Spectral methods have aroused great interest in approximating numerically a smooth problem for their attractive geometric convergence rates. The geometric numerical methods are praised for their excellent long-time geometric structure-preserving properties. According to the generalized Galerkin framework, we combine two methods together to construct a variational integrator, which captures the merits of both methods. Since the interpolating points of the variational integrator are chosen as the Chebyshev points, the integration of Lagrangian can be approximated by the Clenshaw-Curtis quadrature rule, and the barycentric Lagrange interpolation is presented to substitute for the classic Lagrange interpolation in the approximation of configuration variables and the corresponding derivatives. The numerical float errors of the first-order spectral differentiation matrix can be alleviated by using a trigonometric identity especially when the number of Chebyshev points is large. Furthermore, the spectral variational integrator (SVI) constructed by the Gauss-Legendre quadrature rule and the multi-interval spectral method are carried out to compare with the CSVI, and the interesting kink phenomena for the Clenshaw-Curtis quadrature rule are discovered. The numerical results reveal that the CSVI has an advantage on the computing time over the whole progress and a higher accuracy than the SVI before the kink position. The effectiveness of the proposed method is demonstrated and verified perfectly through the numerical simulations for several classical mechanics examples and the orbital propagation for the planet systems and the Solar system.

Key words geometric numerical method, spectral method, variational integrator, Clenshaw-Curtis quadrature rule, barycentric Lagrange interpolation, orbital propagation

Chinese Library Classification O302, P138$^+$.2
2010 Mathematics Subject Classification 74H40, 70F10

* Citation: YI, Z. G., YUE, B. Z., and DENG, M. L. Chebyshev spectral variational integrator and applications. *Applied Mathematics and Mechanics* (*English Edition*), **41**(5), 753–768 (2020) https://doi.org/10.1007/s10483-020-2602-8

† Corresponding author, E-mail: bzyue@bit.edu.cn

Project supported by the National Natural Science Foundation of China (Nos. 11472041, 11532002, 11772049, and 11802320)

1 Introduction

During the past decade, the development of geometric numerical methods has been of particular interest in numerical integration methods. The geometric numerical methods are praised for their excellent long-time geometric structure-preserving properties, such as the energy and momentum conservation behaviors, and the symplectic-preserving property[1–2]. The variational integrator is a kind of popular geometric numerical methods, which can rely on a discrete variational characterization of the underlying systems; that is to say, they are based on a discrete version of Hamilton's principle for the conservative mechanical systems. Generally, there exist two approaches to constructing variational integrators[3–5]. One is the shooting-based construction scheme, which depends on the choice of a numerical quadrature formula together with an underlying one-step method. The other one is the Galerkin construction scheme, which relies on the approximation of the action, and depends on the choice of a numerical quadrature formula and a finite-dimensional function space. The geometric numerical methods have been applied successfully into a variety of fields, for example, the orbital mechanics[6–7], the optimal control problem[8–10], the asteroid exploration[11], the high-order variational integrators on Lie groups[12], and the Birkhoffian systems[13].

Like geometric numerical methods, spectral methods have already captured countless fans in the field of numerical computation in the past decades. One of the most important reasons is that they often possess the capability for achieving geometric rates of convergence, which is faster than any polynomial order. Spectral methods are a large class of methods, which are implemented by choosing a high-dimensional, global function space. In other words, the convergence of the spectral methods is achieved through the dimension n of the function space, not the time-step h. The customary technique of shortening h can often be found in the classic Euler method and Runge-Kutta method. In the classic literature about the spectral methods, Trefethen[14], Boyd[15], Shen et al.[16], Hale and Trefethen[17], and Driscoll et al.[18] presented excellent introductions about the theoretical and practical applications for the spectral methods, which have been further developed and extended to different fields, including the fluid mechanics simulation[19–20] and the optimal control problem for the spacecraft[21–23].

Undeniably, it is really a creative idea for combining the geometric numerical methods together with the spectral methods, and the resulting method can fully inherit the excellent geometric structure-preserving quantities of the geometric numerical methods and the attractive geometric convergence rates of the spectral methods. To this end, Hall and Leok[24] conducted an excellent introduction and a comprehensive geometric convergence analysis and presented the proofs for the spectral variational integrator (SVI). In the work of Hall and Leok, the SVI was constructed through the generalized Galerkin framework, the function space was constructed by a finite set of Lagrange basis functions, and the Lagrangian integrant was approximated by the Gauss-Legendre quadrature formulae, where the number of the quadrature point was not restricted being equal to the order of interpolation polynomial by using different methods from the work of Marsden and West[2]. Finally, they also provided several numerical simulations to verify the theorems of geometric convergence and the long-time geometric structure-preserving behaviors (energy and momentum conservation) of the constructed SVI.

In this paper, the Chebyshev spectral variational integrator (CSVI) is also constructed by the generalized Galerkin framework. Since the interpolating points of the variational integrator are chosen as the Chebyshev points, the integration of Lagrangian can be approximated by "a younger brother" of the Gauss quadrature, i.e., the Clenshaw-Curtis quadrature rule[25], which has essentially the same performance for most integrands. Moreover, the corresponding quadrature weights can be calculated efficiently and effortlessly through the fast Fourier transform (FFT). To improve computational efficiency and numerical stability in the approximation of configuration variables and their derivatives, the classic Lagrange interpolation is replaced by the barycentric Lagrange interpolation[26]. The numerical float errors of the first-order spectral

differentiation matrix can be alleviated by using a trigonometric identity especially when the number of Chebyshev points is large. Furthermore, the SVI constructed by the Gauss-Legendre quadrature rule and the spectral method are presented to compare with the CSVI, and some interesting phenomena of the Clenshaw-Curtis quadrature rule are also discovered. To validate the efficiency of the method presented in this paper, the planar pendulum system and the simplified Kepler two-body system in the classical mechanics are studied firstly as two numerical examples. For the more interesting applications of the methods presented, the orbital propagation problems in the following systems, i.e., the Moon in the Earth-Moon two-body system, the Earth and the Mars in the Sun-Earth-Mars three-body system, and the eight planets and the Pluto in the Solar system, are numerically studied respectively to prove the effectiveness and feasibleness of the present method.

The structure of this paper is organized as follows. In Section 2, the basic concepts of the discrete mechanics and the variational integrators are reviewed briefly. Section 3 conducts the implementing details of the CSVI. In Section 4, several numerical simulation results are performed. The last section presents some conclusions.

2 Discrete variational mechanics

Firstly, we would like to review briefly some basic concepts and definitions for the discrete mechanics and variational integrators[2,24], which are used in this paper. Also, a theorem of geometric convergence for the discrete geometric spectral method is presented.

2.1 Discrete mechanics

Consider a mechanical system defined on the n-dimensional configuration manifold Q with time-dependent curves $\boldsymbol{q}(t) \in Q,\ t \in [t_0, t_\mathrm{f}]$. The associated state space of the manifold Q is given by the tangent bundle TQ, and the associated phase space is defined by the cotangent bundle T^*Q. The corresponding Lagrangian $L : TQ \to \mathbb{R}$ is described by the kinetic energy minus potential energy. Then, the action $\mathfrak{S} : C^2([t_0, t_\mathrm{f}], Q) \to \mathbb{R}$ of the proposed mechanical system is defined as follows:

$$\mathfrak{S}(\boldsymbol{q}) = \int_{t_0}^{t_\mathrm{f}} L(\boldsymbol{q}(t), \dot{\boldsymbol{q}}(t))\mathrm{d}t. \tag{1}$$

However, in discrete mechanics, the total time interval $t \in [t_0, t_\mathrm{f}]$ is divided into N uniform-space subintervals, and the corresponding step-size is denoted by h. Considering the kth time grid $[t_0 + kh, t_0 + (k+1)h],\ k = 0, 1, \cdots, N-1$, the discrete Lagrangian $L_\mathrm{d} : Q \times Q \times \mathbb{R} \to \mathbb{R}$ is defined through the discrete state space $Q \times Q$ to approximate the exact discrete Lagrangian, i.e.,

$$L_\mathrm{d}(\boldsymbol{q}_k, \boldsymbol{q}_{k+1}, h) \approx L_\mathrm{d}^\mathrm{E}(\boldsymbol{q}_k, \boldsymbol{q}_{k+1}, h) = \int_{t_k}^{t_{k+1}} L(\boldsymbol{q}(t), \dot{\boldsymbol{q}}(t))\mathrm{d}t, \tag{2}$$

where L_d^E is associated with Jacobi's solution of the Hamilton-Jacobi equation for a sufficiently small h, which generally is not computable.

Therefore, on the total time interval $t \in [t_0, t_\mathrm{f}]$, the discrete action $\mathfrak{S}_\mathrm{d} : Q^{N+1} \to \mathbb{R}$ can be approximated by the sum of the discrete Lagrangian on each two neighboring discrete configurations $\boldsymbol{q}_k$ and $\boldsymbol{q}_{k+1}$, i.e.,

$$\mathfrak{S}_\mathrm{d}(\boldsymbol{q}_0, \boldsymbol{q}_1, \cdots, \boldsymbol{q}_N) = \sum_{k=0}^{N-1} L_\mathrm{d}(\boldsymbol{q}_k, \boldsymbol{q}_{k+1}). \tag{3}$$

Then, according to Hamilton's principle, the true trajectory should satisfy the stationary point conditions of the discrete action, i.e.,

$$\delta\mathfrak{S}_\mathrm{d}(\boldsymbol{q}_0, \boldsymbol{q}_1, \cdots, \boldsymbol{q}_N) = 0 \tag{4}$$

for all variations $\delta \boldsymbol{q}_k$, which will vanish at the fixed end-points (i.e., $\delta \boldsymbol{q}_0 = \delta \boldsymbol{q}_N = 0$). This would lead to the discrete Euler-Lagrange equations,

$$\mathrm{D}_1 L_\mathrm{d}(\boldsymbol{q}_k, \boldsymbol{q}_{k+1}) + \mathrm{D}_2 L_\mathrm{d}(\boldsymbol{q}_{k-1}, \boldsymbol{q}_k) = 0 \tag{5}$$

for $k = 0, 1, \cdots, N-1$, where D_1 and D_2 denote partial derivatives with respect to the first and second arguments of L_d, respectively.

Equation (5) provides an implicit one-step iteration map for a given pair $\boldsymbol{q}_{k-1}$ and $\boldsymbol{q}_k$, known as the discrete Lagrangian flow map F_{L_d}: $Q \times Q \to Q \times Q$, i.e., $F_{L_\mathrm{d}}(\boldsymbol{q}_{k-1}, \boldsymbol{q}_k) = (\boldsymbol{q}_k, \boldsymbol{q}_{k+1})$. This one-step update schemes derived by a discrete variational principle are referred to as variational integrators, which are well-known to be symplectic and momentum-preserving and exhibit excellent long-time energy behaviors.

We know that the Lagrangian can be associated with the Hamiltonian through the continuous Legendre transforms. However, this relationship is also true under the discrete cases. The discrete Legendre transform $\mathbb{F}^{\pm} L_\mathrm{d} : Q \times Q \to T^*Q$ can then be defined by the transformation of discrete Lagrangian,

$$\mathbb{F}^- L_\mathrm{d} : (\boldsymbol{q}_k, \boldsymbol{q}_{k+1}) \to (\boldsymbol{q}_k, \boldsymbol{p}_k^-) = (\boldsymbol{q}_k, -\mathrm{D}_1 L_\mathrm{d}(\boldsymbol{q}_k, \boldsymbol{q}_{k+1})), \tag{6}$$

$$\mathbb{F}^+ L_\mathrm{d} : (\boldsymbol{q}_{k-1}, \boldsymbol{q}_k) \to (\boldsymbol{q}_k, \boldsymbol{p}_k^-) = (\boldsymbol{q}_k, \mathrm{D}_2 L_\mathrm{d}(\boldsymbol{q}_{k-1}, \boldsymbol{q}_k)). \tag{7}$$

Using the discrete Legendre transforms, we can define the discrete Hamiltonian flow map $\widetilde{F}_{L_\mathrm{d}} : T^*Q \to T^*Q$ as follows:

$$\widetilde{F}_{L_\mathrm{d}} : (\boldsymbol{q}_k, \boldsymbol{p}_k) \to (\boldsymbol{q}_{k+1}, \boldsymbol{p}_{k+1}) = \mathbb{F}^+ L_\mathrm{d} \circ (\mathbb{F}^- L_\mathrm{d})^{-1}(\boldsymbol{q}_k, \boldsymbol{p}_k), \tag{8}$$

which is equivalent to the discrete Lagrangian flow map. For a more detailed illustration of the commutative relationship among the discrete Hamiltonian flow map, the discrete Lagrangian flow map, and the discrete Legendre transforms, we recommend Refs. [2] and [24] for a thorough introduction.

2.2 Variational integrators

According to the generalized Galerkin framework, the variational integrators can be constructed through two steps, which are discussed thoroughly by Marsden and West[2] and Hall and Leok[24].

The first step is to approximate the discrete action $\mathfrak{S}_\mathrm{d}\left(\{q_k\}_{k=0}^n\right)$, which consists of the approximation of the space of trajectories through a finite-dimensional function space and the approximation of the integral of the Lagrangian on a certain subinterval through appropriate quadrature rules. That is to say, we need to employ a highly-accurate computable discrete Lagrangian $L_\mathrm{d}(\boldsymbol{q}_k, \boldsymbol{q}_{k+1})$ to approximate the general numerically non-computable exact discrete Lagrangian $L_\mathrm{d}^\mathrm{E}(\boldsymbol{q}_k, \boldsymbol{q}_{k+1})$. Specifically, for a given subinterval $[t_0 + kh, t_0 + (k+1)h]$, $k = 0, 1, \cdots, N-1$, and Lagrangian $L : TQ \to \mathbb{R}$, the approximate procedure is constructed as follows.

(i) Choose an $(n+1)$-dimensional function space to approximate the space of trajectories: $\mathbb{M}^n\left([t_0 + kh, t_0 + (k+1)h],\ Q\right) \subset C^2\left([t_0 + kh, t_0 + (k+1)h],\ Q\right)$ with a finite set of basis functions $\{l_{v,n}(t)\}_{v=0}^n$, these basis functions are generated by Lagrange basis polynomials and shall be extended in Subsection 3.1.

(ii) Choose a quadrature rule (ω_i, τ_i) to approximate the integral of the Lagrangian in Eq. (2), i.e.,

$$L_\mathrm{d}(\boldsymbol{q}_k = \boldsymbol{q}_k^0, \boldsymbol{q}_k^1, \cdots, \boldsymbol{q}_k^n = \boldsymbol{q}_{k+1}, h) \approx \operatorname*{ext}_{\substack{\boldsymbol{q} \in \mathbb{M}^n([t_0+kh, t_0+(k+1)h),\ Q) \\ \boldsymbol{q}_k = \boldsymbol{q}_k^0, \boldsymbol{q}_k^n = \boldsymbol{q}_{k+1}}} \frac{h}{2} \sum_{\mu=1}^{n} \omega_\mu L(\boldsymbol{q}(\tau_\mu), \dot{\boldsymbol{q}}(\tau_\mu)), \tag{9}$$

which would be expanded and discussed carefully in Subsection 3.2.

Then, the next step is to conduct a variation operating (finding an extremizer) for the discrete action $\mathfrak{S}_{\mathrm{d}}$ through the discrete Hamilton's principle, which requires that the curve $\boldsymbol{q}_k^v, v = 1, 2, \cdots, n-1$ should be a stationary point of the discretized action. This leads to $n-1$ internal stage conditions,

$$\mathrm{D}_v L_{\mathrm{d}}(\boldsymbol{q}_k = \boldsymbol{q}_k^0, \boldsymbol{q}_k^1, \cdots, \boldsymbol{q}_k^n = \boldsymbol{q}_{k+1}, h) = \boldsymbol{0}, \quad v = 1, 2, \cdots, n-1, \tag{10}$$

where D_v denotes the partial derivative with respect to $\boldsymbol{q}_k^v$. Combining these internal stage conditions with the implicit one-step iteration map (i.e., Euler-Lagrange equations) yields a set of $n+1$ nonlinear equations,

$$\sum_{\mu=1}^{n} \omega_\mu \Big(\frac{h}{2} l_{0,n}(\tau_\mu) \frac{\partial L}{\partial \boldsymbol{q}}(\tau_\mu) + \dot{l}_{0,n}(\tau_\mu) \frac{\partial L}{\partial \dot{\boldsymbol{q}}}(\tau_\mu) \Big) = \mathrm{D}_1 L_{\mathrm{d}}(\boldsymbol{q}_k, \boldsymbol{q}_{k+1}) = -\boldsymbol{p}_k, \tag{11a}$$

$$\mathrm{D}_v L_{\mathrm{d}}(\boldsymbol{q}_k = \boldsymbol{q}_k^0, \boldsymbol{q}_k^1, \cdots, \boldsymbol{q}_k^n = \boldsymbol{q}_{k+1}, h) = \boldsymbol{0}, \quad v = 1, 2, \cdots, n-1, \tag{11b}$$

$$\sum_{\mu=1}^{n} \omega_\mu \Big(\frac{h}{2} l_{n,n}(\tau_\mu) \frac{\partial L}{\partial \boldsymbol{q}}(\tau_\mu) + \dot{l}_{n,n}(\tau_\mu) \frac{\partial L}{\partial \dot{\boldsymbol{q}}}(\tau_\mu) \Big) = \mathrm{D}_2 L_{\mathrm{d}}(\boldsymbol{q}_k, \boldsymbol{q}_{k+1}) = \boldsymbol{p}_{k+1}. \tag{11c}$$

For a given pair $(\boldsymbol{q}_k = \boldsymbol{q}_k^0, \boldsymbol{p}_k)$ on the subinterval $(t_0+kh, t_0+(k+1)h),\ k = 0, 1, \cdots, N-1$, we can obtain the solution sequences $(\{\boldsymbol{q}_k^v\}_{v=1}^n)$ by solving Eqs. (11a) and (11b). Then, $(\boldsymbol{q}_{k+1}, \boldsymbol{p}_{k+1})$ can be updated by using the relation $\boldsymbol{q}_{k+1} = \boldsymbol{q}_k^n$ and evaluating Eq. (11c), respectively. And this yields the discrete Hamiltonian flow map $\widetilde{F}_{L_{\mathrm{d}}} : (\boldsymbol{q}_k, \boldsymbol{p}_k) \mapsto (\boldsymbol{q}_{k+1}, \boldsymbol{p}_{k+1})$. Then, similar pair evaluating can be updated on the whole time interval. However, in the practical problems, the initial conditions of a mechanics system are generally given directly in terms of position and velocity $(\boldsymbol{q}_0, \boldsymbol{v}_0) \in TQ$. Then, one is supposed to convert them into the form of position and momentum on the cotangent bundle (i.e., $(\boldsymbol{q}_0, \boldsymbol{p}_0) \in T^*Q$) by employing the continuous Legendre transform $\mathbb{F}L : TQ \to T^*Q,\ (\boldsymbol{q}_0, \boldsymbol{v}_0) \to (\boldsymbol{q}_0, \boldsymbol{p}_0) = (\boldsymbol{q}_0, \frac{\partial L}{\partial \dot{\boldsymbol{q}}}(\boldsymbol{q}_0, \boldsymbol{v}_0))$.

2.3 Geometric convergence property

Here, a description of the geometric convergence of discrete geometric spectral method is presented. We refer the interested reader to the literature of Hall and Leok[24] for a celebrated description and a rigorous proof process.

Theorem 1 *Given a Lagrangian $L : TQ \to \mathbb{R}$ and a time interval $[t_k, t_{k+1}]$, assume that all partial derivatives of L are continuous on a closed and bounded neighborhood $U \in TQ$ (i.e., L is Lipschitz continuous on U); the spectral variational discrete solutions of the trajectories on the tangent space TQ have an error bounded by $C_{\mathrm{A}} K_{\mathrm{A}}^n$ for some constants C_{A} and K_{A} ($K_{\mathrm{A}} < 1$), which are independent of n; the chosen discrete quadrature rule for approximating the discrete Lagrangian L_{d} has an error bounded by $C_{\mathrm{g}} K_{\mathrm{g}}^n$ for some constants C_{g} and K_{g} ($K_{\mathrm{g}} < 1$), which are independent of n as well. Then, a geometric convergence boundary can be drawn as*[24]

$$|L_{\mathrm{d}}^{\mathrm{E}}(\boldsymbol{q}_k, \boldsymbol{q}_{k+1}) - L_{\mathrm{d}}(\boldsymbol{q}_k, \boldsymbol{q}_{k+1})| \leqslant C_{\mathrm{s}} K_{\mathrm{s}}^n$$

for some constants C_{s} and K_{s} ($K_{\mathrm{s}} = \max(K_{\mathrm{A}}, K_{\mathrm{g}}), K_{\mathrm{s}} < 1$), which are independent of n. That is to say, the discrete Hamiltonian flow map $\widetilde{F}_{L_{\mathrm{d}}} : (\boldsymbol{q}_k, \boldsymbol{p}_k) \mapsto (\boldsymbol{q}_{k+1}, \boldsymbol{p}_{k+1})$ has an error $O(K_{\mathrm{s}}^n)$.

3 Spectral approximation

In this section, we will discuss how to employ a chosen spectral method to construct an approximation for the discrete action $\mathfrak{S}_{\mathrm{d}}$ introduced in Eq. (3) and Subsection 2.2.

3.1 Barycentric Lagrange interpolation

Without loss of generality, we firstly consider a given time subinterval $[t_0 + kh, t_0 + (k + 1)h]$, $k = 0, 1, \cdots, N-1$ on the total time interval $t \in [t_0, t_{\rm f}]$, which is divided into N uniform-space subintervals, and the corresponding step-size is h.

As stated in Subsection 2.2, the $(n+1)$-dimensional function space is generated by a finite set of Lagrange interpolation polynomials $\{l_{v,n}(t)\}_{v=0}^{n}$, where the control points are chosen as the Chebyshev points $\tau \in [-1, 1]$ in this paper as follows:

$$\tau_i = \cos\Big(\frac{(n-i)\pi}{n}\Big), \quad i = 0, 1, \cdots, n. \tag{12}$$

This type of point sets is clustered at the boundary of the interval $[-1, 1]$ with an asymptotic density proportional to $(1-\tau^2)^{-1/2}$ as $n \to \infty$[14], and it can avoid effectively the Runge phenomenon that often occurs in the case of uniform-density distribution points, as shown in Fig. 1. Therefore, the subinterval $t \in [t_k, t_{k+1}]$, $k = 0, 1, \cdots, N-1$ can be projected to this kind of distribution on the interval $[-1, 1]$ by the transformation $t = \frac{(t_k+t_{k+1})}{2} - \frac{(t_k-t_{k+1})}{2\tau}$.

From the procedure (i) in Subsection 2.2, we know that a basis function of $(n+1)$-order Lagrange interpolation polynomials is chosen to approximate the state variables of the space of trajectories,

$$\boldsymbol{q}(\tau) \approx \sum_{v=0}^{n} l_{v,n}(\tau)\boldsymbol{q}_k^v, \tag{13}$$

where the classic Lagrange interpolation polynomials are defined traditionally as[4,22,27–28]

$$l_{{\rm c},v,n}(\tau) = \prod_{\mu=0,\mu\neq v}^{n} \frac{(\tau-\tau_\mu)}{(\tau_v-\tau_\mu)}, \quad v = 0, 1, \cdots, n. \tag{14}$$

However in this paper, in order to improve the computational efficiency and numerical stability, the barycentric Lagrange interpolation is used to substitute for the classic Lagrange interpolation, which may not be familiar to many people but "deserves a place at the heart of introductory courses and textbooks in the numerical analysis"[26],

$$l_{v,n}(\tau) = \frac{\frac{\xi_v}{\tau-\tau_v}}{\sum\limits_{\mu=0}^{n}\frac{\xi_\mu}{\tau-\tau_\mu}}, \quad v = 0, 1, \cdots, n, \tag{15}$$

where the barycentric weights ξ_v are defined as $\xi_v = 1\Big/\Big(\prod\limits_{\mu=0,\mu\neq v}^{n}(\tau_v-\tau_\mu)\Big)$, $v = 0, 1, \cdots, n$. It can be found in the denominator that the calculation of $(\tau_v - \tau_\mu)$ would lead to floating-point cancellation errors for a large n. Here, an effective method is presented[22,26],

$$\xi_v = \begin{cases} \dfrac{(-1)^v}{2}, & v = 0 \quad \text{or} \quad v = n, \\ (-1)^v, & \text{otherwise.} \end{cases} \tag{16}$$

However, here we must make a remark: this formula can only be used under a condition that ξ_v can occur in the numerator and denominator at the same time; for example, it is true in Eq. (15) but not in the original equation of ξ_v. It results from employing the Chebyshev points.

According to Eq. (13), the velocity variables of the space of trajectories can be approximated as

$$\dot{\boldsymbol{q}}(\tau) \approx \sum_{v=0}^{n} \dot{l}_{v,n}(\tau)\boldsymbol{q}_k^v, \tag{17}$$

where the element of the differential matrix can be written as[26]

$$D_{k,v} = \dot{l}_{v,n}(\tau_k) = \begin{cases} \dfrac{\frac{\xi_v}{\xi_k}}{\tau_k - \tau_v}, & k \neq v, \\ -\sum\limits_{j=0, j\neq k}^{n} D_{k,j}, & k = v, \end{cases} \tag{18}$$

which has a better numerical stability than Eq. (28) of Ref. [22] and Eq. (5) of Ref. [29], and ξ_v and ξ_k can be calculated efficiently by Eq. (16).

3.2 Clenshaw-Curtis quadrature rule

As stated in Eq. (9), a quadrature rule (ω_i, τ_i) is chosen to approximate the integral of the Lagrangian in Eq. (2). In this paper, "a younger brother" of the Gauss quadrature, the Clenshaw-Curtis quadrature rule[25], is used to conduct such tasks, which has essentially the same performance as the Gauss quadrature for most integrands. Moreover, the corresponding quadrature weights can be calculated efficiently and effortlessly through the FFT. A comparison simulation with the Gauss-Legendre quadrature rule is conducted in Fig. 2.

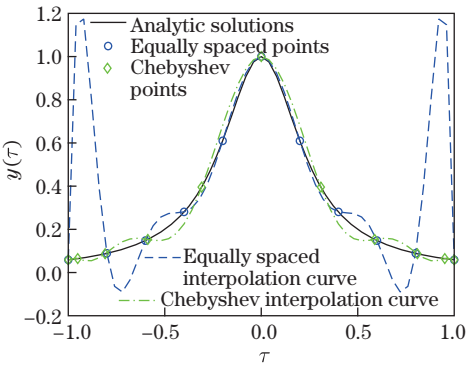

Fig. 1 The Runge phenomenon of barycentric Lagrange interpolation for $y(\tau) = 1/(1+16\tau^2)$ is presented. The curve oscillates at the values about 2^n times larger near $\tau = \pm 1$ than those near $\tau = 0$ for equally spaced points, while the curve oscillates between the values on the order of 2^{-n} over $[-1, 1]$ for the Chebyshev points[14]. Besides, a failure of $\tau - \tau_i$ in Eq. (15) should be treated carefully (color online)

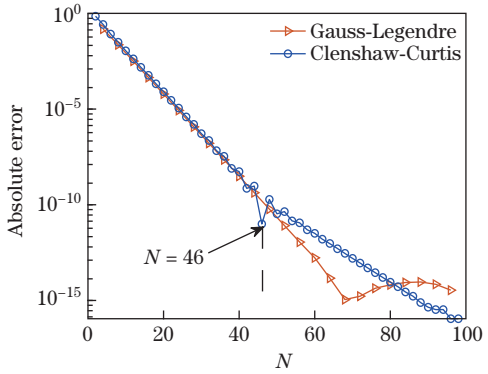

Fig. 2 The kink phenomenon of the Clenshaw-Curtis quadrature rule for $f(\tau) = \int_{-1}^{1} 1/(1+16\tau^2)\mathrm{d}\tau$ is presented. It can be found that the Clenshaw-Curtis quadrature has the close convergence rate with its "older brother" Gauss-Legendre quadrature formula for smaller n. A complete description and the error formulae are provided in Ref. [30] to explain the kink phenomenon for larger n (color online)

For the fast construction of weights of Clenshaw-Curtis quadrature rule, a new method (the discrete cosine transform and discrete sine transform)[31] is presented to compute the weights. However, in our paper, an elegant algorithm for stably and quickly generating the weights is constructed through the FFT[32], and the weights ω_k^{cc} of Clenshaw-Curtis quadrature formulae can be written as follows:

$$\omega_k^{\mathrm{cc}} = \begin{cases} \omega_k^{\mathrm{F}_2} + \dfrac{c_k(-1)^k}{n^2-1}, & n \text{ is even}, \\ \omega_k^{\mathrm{F}_2} + \dfrac{c_k(-1)^k}{n^2}\cos\left(\dfrac{k\pi}{n}\right), & n \text{ is odd}, \end{cases} \tag{19}$$

where $\omega_k^{\mathrm{F}_2}$ represents the Fejér-2 quadrature weight $\omega_k^{\mathrm{F}_2} = F_n^{-1} v_k$[22], F_n^{-1} represents the inverse FFT (IFFT), and v_k is defined as follows:

$$\begin{cases} v_k = \dfrac{2}{1-4k^2}, \quad k = 0, 1, \cdots, \left[\dfrac{n}{2}\right] - 1, \\ v_{[n/2]} = \dfrac{n-3}{2[n/2]-1} - 1, \\ v_{n-k} = v_k, \quad k = 1, 2, \cdots, \left[\dfrac{n-1}{2}\right], \end{cases} \tag{20}$$

which holds for all positive integers $n > 1$[32]. $\omega_n^{\mathrm{F}_2} = \omega_0^{\mathrm{F}_2} = 0$. c_k in Eq. (19) is defined by $c_k = 1$ for $k = 0$ or n, while $c_k = 2$ for other k.

A simplification of Eq. (19) would lead to a practical formula $\omega_k^{\mathrm{cc}} = F_n^{-1}(v_k + g_k)$, where in analogy to v_k, g_k is written as follows[32]:

$$\begin{cases} g_k = -\omega_0^{\mathrm{cc}}, \quad k = 0, 1, \cdots, \left[\dfrac{n}{2}\right] - 1, \\ g_{[n/2]} = \omega_0^{\mathrm{cc}} \left[(2 - \mathrm{mod}(n, 2))n - 1\right], \\ g_{n-k} = v_k, \quad k = 1, 2, \cdots, \left[\dfrac{n-1}{2}\right], \end{cases} \tag{21}$$

where ω_0^{cc} is presented by $\omega_0^{\mathrm{cc}} = 1/(n^2 - 1 + \mathrm{mod}(n, 2))$. Finally, we should set $\omega_n^{\mathrm{cc}} = \omega_0^{\mathrm{cc}}$.

4 Numerical analysis

This section presents the numerical simulations for several different questions to verify the effectiveness and convergence of the constructed algorithm. As a well-known and classical mechanics problem for periodic motion, which can illustrate perfectly the favorable long-time structure-preserving behaviors (e.g., energy and momentum conservation) of geometric methods, the planar pendulum system and the Kepler two-body problem are performed as the first and second simulations, respectively. Moreover, the orbital propagations of the Earth-Moon and the Sun-Earth-Mars systems are also studied in the third numerical experiment as an application. At last, the Solar system's orbital propagation is also simulated as another application in this paper.

In order to compare the CSVI constructed by the barycentric Lagrange interpolation and the Clenshaw-Curtis quadrature rule in this paper, the method introduced in Refs. [24] and [27] is also presented, which employs the classical Lagrange interpolation and Gauss-Legendre quadrature rule to do such work. The difference is the number of the interpolating points (i.e., Chebyshev points), the interpolating points are twice as many as the quadrature points in Refs. [24] and [27]. However, it is chosen as the same number of quadrature point in this paper. On the other hand, the CSVI combines the geometric numerical methods together with the spectral methods, and the resulting combination can fully inherit the excellent geometric structure-preserving quantities and the attractive geometric convergence of the spectral methods. Therefore, the spectral method is also carried out. However, it is not the focus of this paper, and we refer the interested readers to Refs. [14]–[16] and [27]. A modification of the spectral method should be pointed out, i.e., the interpolation is performed by the barycentric Lagrange interpolation, the differential matrix is evaluated by Eq. (18), and the multi-interval spectral method is employed.

All the algorithms are conducted by MATLAB 2018b genuine software and performed on a computer of Inter i7-8700k@3.70 GHz, RAM 16.0 GB. The nonlinear equations are solved by the Newton-Raphson method, where the maximum iteration number is set as 1 000, and the iteration error threshold is set as $\varepsilon = 10^{-12}$. The algorithms typically converge among 5 iterations for each subinterval in this paper.

4.1 Planar pendulum

Firstly, we consider a simple example for the constructed algorithm to illustrate its effectiveness. Consider a pendulum moving on a vertical plane in the gravity field, and the Lagrangian $L : TQ \to \mathbb{R}$ can be defined by the kinetic energy minus potential energy of the system,

$$L(q, \dot{q}) = \frac{1}{2} m (l\dot{q})^2 + mgl \cos q, \tag{22}$$

where $q \in S^1$ represents the angle of the non-mass rigid-rod with the length l relative to the direction of gravity, m is the mass, and g denotes the gravity acceleration.

According to the continuous Legendre transform and Hamilton's principle, the corresponding Euler-Lagrange equation and Hamilton's canonical equation are respectively given by

$$\begin{cases} \ddot{q} + \dfrac{g}{l} \sin q = 0, \\ \dot{q} = \dfrac{p}{ml^2}, \quad \dot{p} = -mgl \sin q. \end{cases} \tag{23}$$

Conducting an energy transformation for Eq. (23) would yield a set of trajectory on the phase space, as shown in Fig. 3, where we assume that $m = g = l = 1$ for simplicity, and C_{E} represents the integral constant.

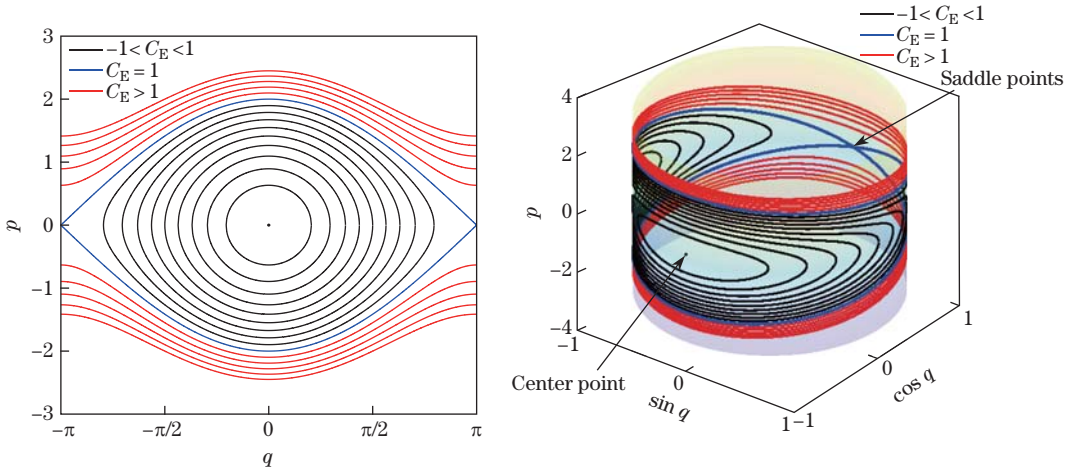

(a) Planar phase diagram (b) Space phase diagram

Fig. 3 The phase diagrams of the planar pendulum (color online)

Therefore, the period is 2π, and the energy is $E = \frac{p^2}{2} - \cos q$. Then, the numerical simulation is conducted on 100 periods (i.e., $t_0 = 0, t_{\mathrm{f}} = 200\pi$), the time-step is set as $h = 0.5$, and the initial point is chosen as $(q_0, p_0) = (\pi/3, 0)$. For the CSVI, the interpolation points are chosen as 4 Chebyshev points (i.e., $n = 3$ in Eq. (12)). For the SVI presented in Refs. [24] and [27], the interpolation points are set as 4 Chebyshev points, and 4 points of Gauss-Legendre quadrature (including two end-points) for comparison. For the multi-interval spectral method (actually, it is an improved method of the pseudospectral method (PM)), the interpolation points are also 4 Chebyshev points. The simulating results are presented in Fig. 4.

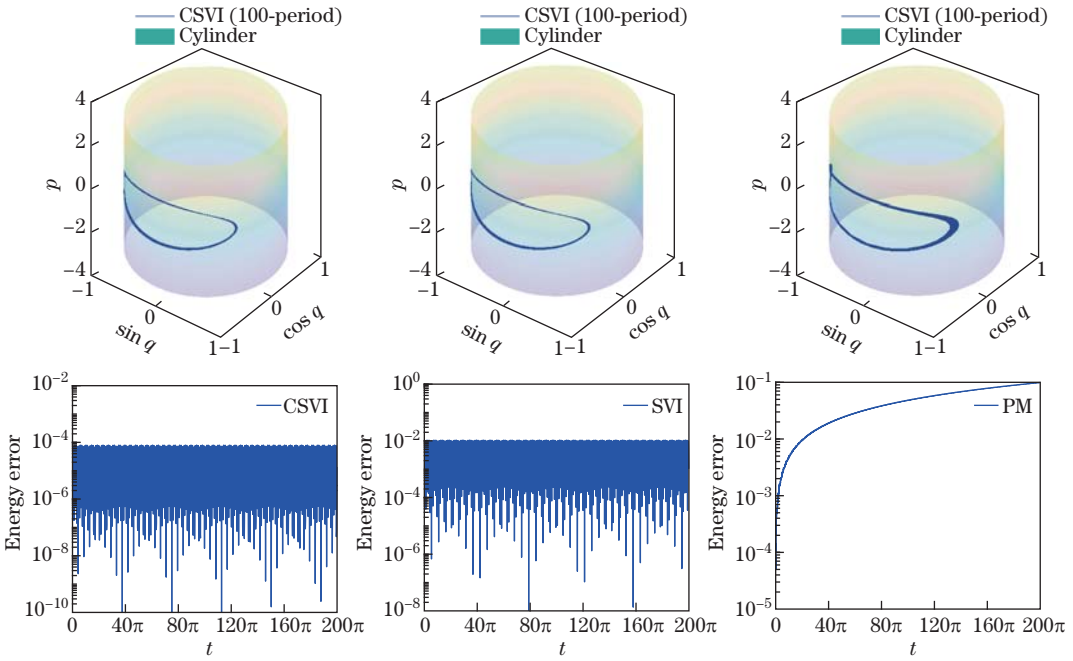

(a) Results of CSVI for 4 Chebyshev points

(b) Results of SVI for 4 Chebyshev points and 4 Gauss-Legendre points

(c) Results of PM for 4 Chebyshev points

Fig. 4 The phase diagrams and the energy errors of the planar pendulum for step-size $h = 0.5$ and $t_{\mathrm{f}} = 200\pi$ (color online)

According to the results of the simulation in Fig. 4, we can see that the CSVI constructed in this paper is reasonable and excellent, and it possesses the long-time structure-preserving behaviors and has a higher convergence precision than the spectral variational method approximated by the Gauss-Legendre quadrature rule. While the spectral method gives a worse result, the phase diagram is divergent, and so is the energy error.

4.2 Kepler two-body problem

As a classical and interesting mechanics problem, the Kepler N-body problem always occurs in the researches of aerospace engineering, mechanics, mathematics, nonlinear analysis fields, etc. Of course, it is still a problem that has not yet solved even for the three-body problem. The Lagrangian for the Kepler N-body problem can be defined by the kinetic energy minus potential energy[24],

$$L(\boldsymbol{q}, \dot{\boldsymbol{q}}) = \frac{1}{2}\sum_{i=1}^{N} \dot{\boldsymbol{q}}^{\mathrm{T}} \boldsymbol{M} \dot{\boldsymbol{q}} + G\sum_{i=1}^{N}\sum_{j=0}^{i-1} \frac{m_i m_j}{\|q_i - q_j\|}, \tag{24}$$

where q_i denotes the mass center of body i, $\boldsymbol{M}$ is the mass matrix consisting of body m_i, and G is the universal gravitational constant.

For simplicity, we firstly consider the Kepler two-body problem and set $m_1 = m_2 = G = 1$, and choose the perifocal coordinate system (i.e., the original point is located at the focal point, the xy-plane coincides with the orbital plane, the x-axis points to the perigee direction, and the y-axis can be obtained by rotating the x-axis 90° along the moving direction). Then, the

energy and angular momentum equations for the Kepler two-body system are written as

$$E(\boldsymbol{q},\boldsymbol{v}) = \frac{1}{2}(v_1^2+v_2^2) - \frac{1}{\sqrt{q_1^2+q_2^2}}, \tag{25}$$

$$M(\boldsymbol{q},\boldsymbol{v}) = q_1 v_2 - q_2 v_1, \tag{26}$$

respectively. Here, the coordinates (q_1, q_2) and (v_1, v_2) denote the position and velocity of the moving-body, respectively. In this numerical experience, the orbital semi-major axis is set as $a = 1$, and the orbital eccentricity is chosen as $e = 0.6$. We choose the perigee point conditions as the initial conditions (i.e., perigee radius and perigee velocity, or in other words, the true anomaly and the eccentric anomaly are equal to zeros at this position),

$$\begin{cases} q_1(0) = \dfrac{a(1-e^2)}{1+e\cos(0)}, \quad q_2(0) = 0, \\ v_1(0) = 0, \quad v_2(0) = \sqrt{\dfrac{\mu}{a}\dfrac{a(1+e)}{a(1-e)}}, \end{cases} \tag{27}$$

where $\mu = Gm_1$ represents the central gravitational constant. According to the energy conservation law and Kepler's third law, the period of the orbit is $T = 2\pi\sqrt{a^3/\mu}$.

Then, the numerical simulations are conducted on 100 periods (i.e., $t_0 = 0, t_{\mathrm{f}} = 200\pi$), and the time-step is set as $h = T/120$. For the CSVI, the interpolation points are chosen as 5 Chebyshev points (i.e., $n = 4$ in Eq. (12)). For the SVI presented in Refs. [24] and [27], the interpolation points are set as 5 Chebyshev points, and 5 points of Gauss-Legendre quadrature (including the end-points) for comparison. For the PM, the interpolation points are also 5 Chebyshev points. For intuition, the solutions to the Kepler equation on one period of the orbit are also iterated and carried out in this paper. The step-size is set as $2h = T/60$. The Newton-Raphson method is used to solve this transcendental equation, and the corresponding maximum iteration number and the iteration error threshold are set as 1 000 and $\varepsilon = 10^{-12}$, respectively. The simulating results are presented in Fig. 5.

It can be found from the results of Fig. 5 that the three methods presented in this paper have a higher precision solution for a smaller interpolation point. Moreover, the CSVI does better than the other two methods on the energy and the angular momentum behaviors. Of course, the PM does not possess the favorable long-time structure-preserving qualities, which can be verified from the third column in Fig. 5. The geometry convergence properties with n-refinement and h-refinement of the Kepler two-body problem are presented in Figs. 6 and 7, respectively.

It can be clearly observed from Fig. 6 that the kink phenomenon occurs in the CSVI, where the Clenshaw-Curtis quadrature rule is employed. For a celebrated description of the kink phenomenon, we refer the interested readers to Ref. [30]. In the front part of the kink, the CSVI has a faster convergence rate than the SVI and the PM. Moreover, the geometry convergence behaviors of the three methods presented in Fig. 6 are consistent with the boundary descriptions in Theorem 1. However, the kink phenomenon disappears in the h-refinement of the CSVI in Fig. 7. The CPU time for h-refinement and n-refinement is presented in Fig. 8, respectively. Finally, it can be summarized that the PM has the lowest accuracy among the three methods, but it has the shortest computing time; the SVI has a more faster convergence speed than the CSVI behind the kink position, while the CSVI also has a faster computing speed over the whole time and the higher accuracy than the SVI before the kink position.

4.3 Planets and Solar system applications

In this numerical example, the geocentric equatorial frame and the heliocentric ecliptic frame are used to describe the moving states for the Earth-Moon two-body system, the Sun-

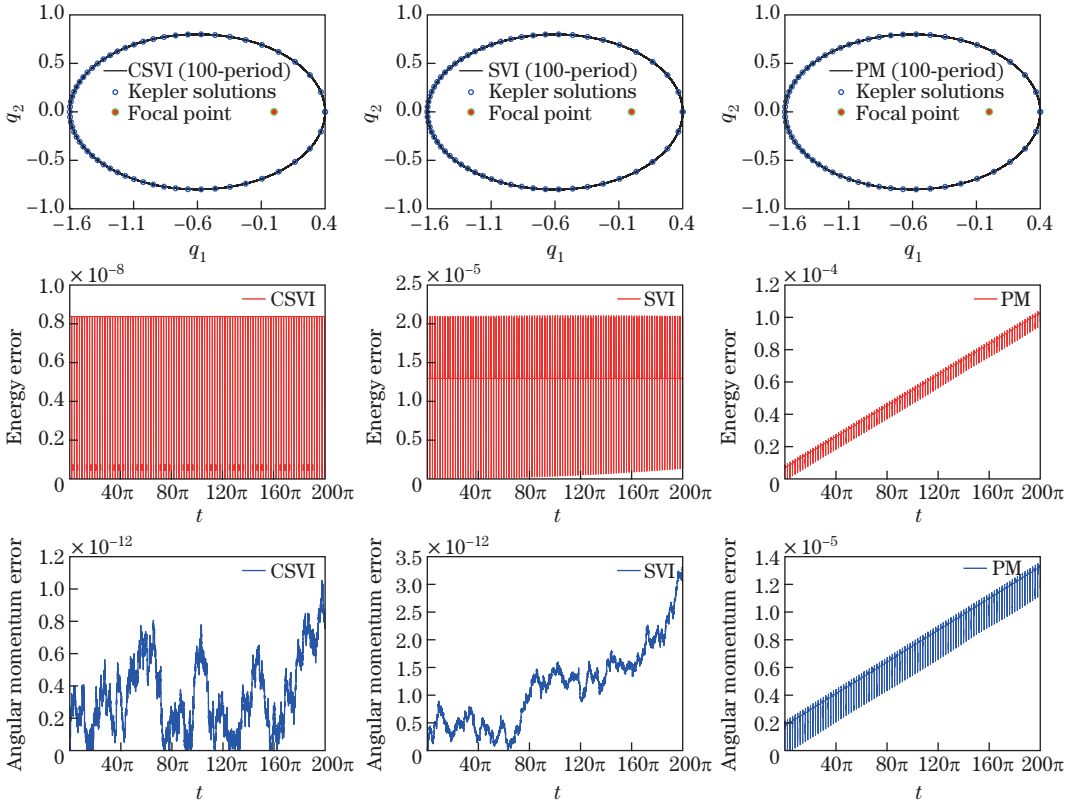

(a) Results of CSVI for 5 Chebyshev points and the same quadrature points

(b) Results of SVI for 5 Chebyshev points and 5 Gauss-Legendre quadrature points

(c) Results of PM for 5 Chebyshev points

Fig. 5 The Kepler two-body problem (color online)

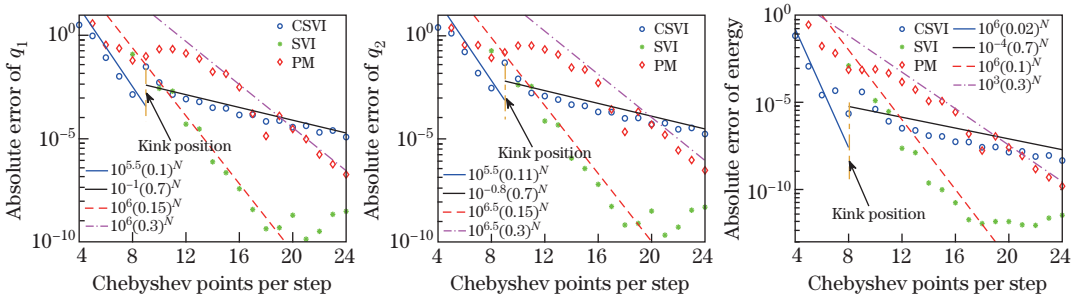

(a) Error curves for the position q_1

(b) Error curves for the position q_2

(c) Error curves for the energy

Fig. 6 The geometry convergences with n-refinement of the Kepler two-body problem with $h = T/12$ over 1 200 steps (color online)

Earth-Mars three-body system, and the Solar system, respectively. The initial configuration parameters (positions and velocities) for the three systems are determined by J2000[24]. The CSVI is applied to three different scenarios. And the corresponding interpolating points and quadrature points are set as $n = 35$ Chebyshev points for the Earth-Moon two-body and the Sun-Earth-Mars three-body systems. As for the Earth-Moon two-body system, the step-size is chosen as $h = 12\,\mathrm{h}$, and a 36 500 d orbit propagation simulation is taken. The integration orbit is presented in Fig. 9. However, a longer time-step $h = 7\,\mathrm{d}$ and a 365 000 d orbit

propagation integration are set for the simulation of the Sun-Earth-Mars three-body system, and the orbital curves described in the heliocentric ecliptic coordinate system are shown in Fig. 10. As for the Solar system, the interpolating points and quadrature points are set as $n = 10$ Chebyshev points, the step-size is chosen as $h = 5\,\mathrm{d}$, and the orbit propagation is

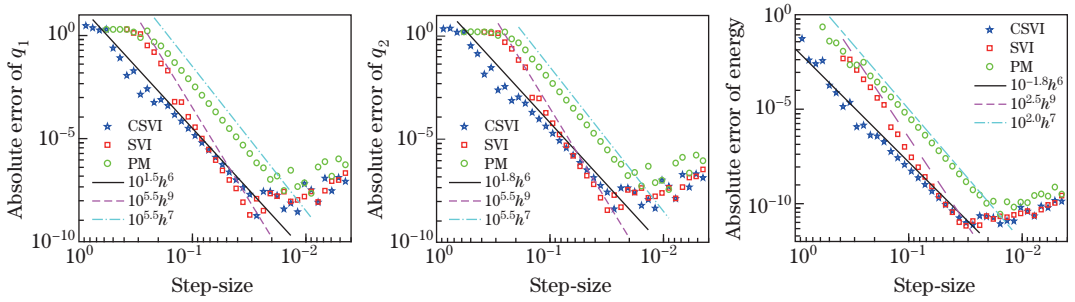

(a) Error curves for the position q_1 (b) Error curves for the position q_2 (c) Error curves for the energy

Fig. 7 The geometry convergences with h-refinement of the Kepler two-body problem with $n = 6$ (color online)

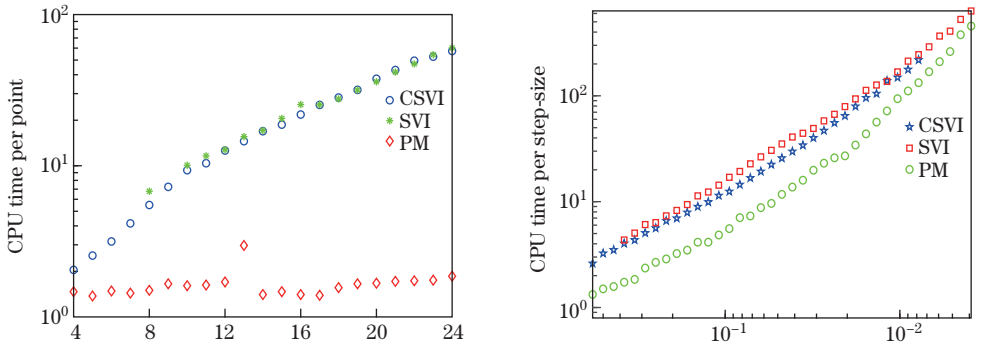

(a) CPU time for n-refinement (b) CPU time for h-refinement

Fig. 8 The CPU time for n-refinement and h-refinement (color online)

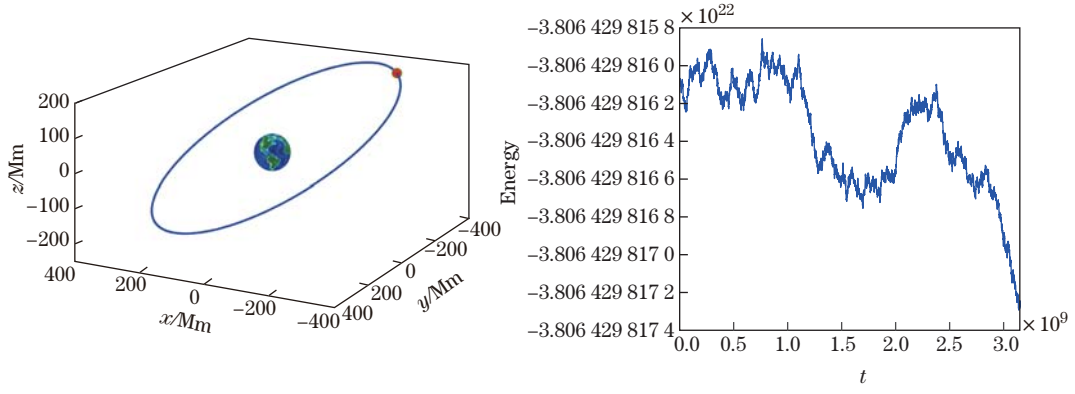

(a) Orbital propagation diagram (b) Energy diagram

Fig. 9 The orbital propagation and energy diagrams of the Earth-Moon two-body system with step-size $h = 12\,\mathrm{h}$ over 36 500 d, which is presented in the geocentric equatorial coordinate system (color online)

taken as 365 000 d. The programs ran about 38.39 h on the above-mentioned computer for the simulation of the Solar system and the integration orbits are presented in Fig. 11.

It can be seen in Figs. 9 and 10, or in Fig. 11 that the orbits are closed, stable for the long-time orbit propagation integration. Moreover, the simulation results do not exhibit the "precession" effect, which often occurs in the symplectic integrator and is a characteristic of this type of integrators. In Fig. 10(b), one can find that this diagram explains perfectly the long-time energy-preserving behavior of the CSVI. In Fig. 11, even though the Pluto only moves about 4 periods in this simulation, the Mercury moves stably about 4 000 periods along its orbit, which means that about 4 000 circles overlap on the green curves in the second picture of Fig. 11. Thus, the simulation results demonstrate the excellent long-time geometric structure-preserving behaviors of the CSVI constructed in this paper.

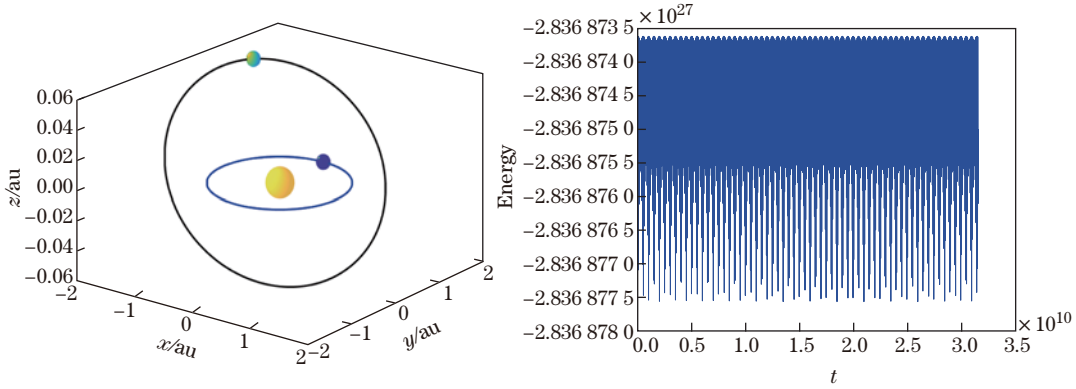

(a) Orbital propagation diagram (b) Energy diagram

Fig. 10 The orbital propagation and energy diagrams of the Sun-Earth-Mars system with step-size $h = 7$ d over 365 000 d, which is described in the heliocentric ecliptic coordinate system, where 1 au $\approx 1.496 \times 10^{11}$ m (color online)

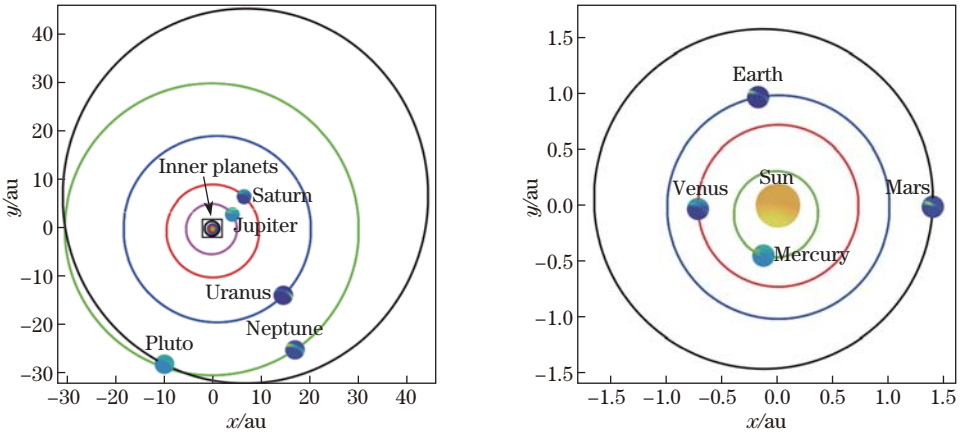

(a) The whole Solar system (b) The inner planets

Fig. 11 The orbital diagrams of the Solar system with step-size $h = 5$ d over 365 000 d are presented. The position for each planet in the above two pictures is the positions in UT: 2000-01-01-12:00:00 (i.e., Julian day: 2 451 545), described in the heliocentric ecliptic coordinate system (color online)

5 Conclusions

This paper studies the CSVI, which possesses excellent long-time structure-preserving behaviors and attractive exponential convergence properties. The multi-interval spectral method and the SVI are presented to compare with the proposed method for the planar pendulum and the Kepler two-body problem. The numerical results reveal that the CSVI has an advantage on the computing time over the whole progress and the higher accuracy than the SVI before the interesting kink position, which is discovered in the n-refinement, but not in the h-refinement. While the multi-interval spectral method is the worst performer in three methods for the accuracy and convergence. Finally, the elegant long-time structure-preserving behavior of the CSVI is verified perfectly by simulating the orbital propagation for the Earth-Moon two-body system, the Sun-Earth-Mars three-body system, and the Solar system.

References

[1] FENG, K. and QIN, M. Z. *Symplectic Geometric Algorithms for Hamiltonian Systems*, Springer, Berlin (2010)

[2] MARSDEN, J. E. and WEST, M. Discrete mechanics and variational integrators. *Acta Numerica*, **10**, 357–514 (2001)

[3] LEOK, M. and SHINGEL, T. General techniques for constructing variational integrators. *Frontiers of Mathematics in China*, **7**(2), 273–303 (2012)

[4] OBER-BLÖBAUM, S. and SAAKE, N. Construction and analysis of higher order Galerkin variational integrators. *Advances in Computational Mathematics*, **41**(6), 955–986 (2015)

[5] LEOK, M. Generalized Galerkin variational integrators. *arXiv*, 0508360 (2005) https://arxiv.org/abs/math/0508360

[6] LEE, T., LEOK, M., and MCCLAMROCH, N. H. Lie group variational integrators for the full body problem in orbital mechanics. *Celestial Mechanics and Dynamical Astronomy*, **98**(2), 121–144 (2007)

[7] PALACIOS, L. and GURFIL, P. Variational and symplectic integrators for satellite relative orbit propagation including drag. *Celestial Mechanics and Dynamical Astronomy*, **130**(4), 31 (2018)

[8] OBER-BLÖBAUM, S., JUNGE, O., and MARSDEN, J. E. Discrete mechanics and optimal control: an analysis. *ESAIM*: *Control*, *Optimisation and Calculus of Variations*, **17**(2), 322–352 (2011)

[9] KOBILAROV, M. B. and MARSDEN, J. E. Discrete geometric optimal control on Lie groups. *IEEE Transactions on Robotics*, **27**(4), 641–655 (2011)

[10] MOORE, A., OBER-BLÖBAUM, S., and MARSDEN, J. E. Trajectory design combining invariant manifolds with discrete mechanics and optimal control. *Journal of Guidance*, *Control*, *and Dynamics*, **35**(5), 1507–1525 (2012)

[11] BOLATTI, D. A. and DE RUITER, A. H. Galerkin variational integrators for orbit propagation with applications to small bodies. *Journal of Guidance*, *Control*, *and Dynamics*, **42**(2), 347–363 (2018)

[12] HALL, J. and LEOK, M. Lie group spectral variational integrators. *Foundations of Computational Mathematics*, **17**(1), 199–257 (2017)

[13] HE, L., WU, H. B., and MEI, F. X. Variational integrators for fractional Birkhoffian systems. *Nonlinear Dynamics*, **87**(4), 2325–2334 (2017)

[14] TREFETHEN, L. N. *Spectral Methods in MATLAB*, Society of Industrial and Applied Mathematics, Philadelphia (2000)

[15] BOYD, J. P. *Chebyshev and Fourier Spectral Methods*, 2nd ed., Dover Publications, Inc., New York (2001)

[16] SHEN, J., TANG, T., and WANG, L. L. *Spectral Methods*: *Algorithms*, *Analysis and Applications*, Springer-Verlag, Berlin (2011)

[17] HALE, N. and TREFETHEN, L. N. Chebfun and numerical quadrature. *Science China Mathematics*, **55**(9), 1749–1760 (2012)

[18] DRISCOLL, T. A., HALE, N., and TREFETHEN, L. N. *Chebfun Guide*, Pafnuty Publications, Oxford (2014)

[19] JIAO, Y. J. and GUO, B. Y. Mixed spectral method for exterior problems of Navier-Stokes equations by using generalized Laguerre functions. *Applied Mathematics and Mechanics* (*English Edition*), **30**(5), 561–574 (2009) https://doi.org/10.1007/s10483-009-0503-z

[20] LI, B. and CHEN, S. Direct spectral domain decomposition method for 2D incompressible Navier-Stokes equations. *Applied Mathematics and Mechanics* (*English Edition*), **36**(8), 1073–1090 (2015) https://doi.org/10.1007/s10483-015-1964-7

[21] GONG, Q., ROSS, I. M., and FAHROO, F. Costate computation by a Chebyshev pseudospectral method. *Journal of Guidance, Control, and Dynamics*, **33**(2), 623–628 (2010)

[22] GE, X. S., YI, Z. G., and CHEN, L. Q. Optimal control of attitude for coupled-rigid-body spacecraft via Chebyshev-Gauss pseudospectral method. *Applied Mathematics and Mechanics* (*English Edition*), **38**(9), 1257–1272 (2017) https://doi.org/10.1007/s10483-017-2236-8

[23] YI, Z. G. and GE, X. S. Attitude maneuver of dual rigid bodies spacecraft using *hp*-adaptive pseudo-spectral method. *International Journal of Aeronautical and Space Sciences*, **20**(1), 214–227 (2019)

[24] HALL, J. and LEOK, M. Spectral variational integrators. *Numerische Mathematik*, **130**(4), 681–740 (2015)

[25] TREFETHEN, L. N. Is Gauss quadrature better than Clenshaw-Curtis? *SIAM Review*, **50**(1), 67–87 (2008)

[26] BERRUT, J. P. and TREFETHEN, L. N. Barycentric Lagrange interpolation. *SIAM Review*, **46**(3), 501–517 (2004)

[27] LI, Y. Q., WU, B. Y., and LEOK, M. Construction and comparison of multidimensional spectral variational integrators and spectral collocation methods. *Applied Numerical Mathematics*, **132**, 35–50 (2018)

[28] LI, Y. Q., WU, B. Y., and LEOK, M. Spectral-collocation variational integrators. *Journal of Computational Physics*, **332**, 83–98 (2017)

[29] LIU, W. J., WU, B. Y., and SUN, J. Some numerical algorithms for solving the highly oscillatory second-order initial value problems. *Journal of Computational Physics*, **276**, 235–251 (2014)

[30] WEIDEMAN, J. A. C. and TREFETHEN, L. N. The kink phenomenon in Fejér and Clenshaw-Curtis quadrature. *Numerische Mathematik*, **107**(4), 707–727 (2007)

[31] SOMMARIVA, A. Fast construction of Fejér and Clenshaw-Curtis rules for general weight functions. *Computers & Mathematics with Applications*, **65**(4), 682–693 (2013)

[32] WALDVOGEL, J. Fast construction of the Fejér and Clenshaw-Curtis quadrature rules. *BIT Numerical Mathematics*, **46**(1), 195–202 (2006)